IEEE TRANSACTIONS ON

MICROWAVE THEORY AND TECHNIQUES

A PUBLICATION OF THE IEEE MICROWAVE THEORY AND TECHNIQUES SOCIETY

MARCH 2008 VOLUME 56 NUMBER 3 IETMAB (ISSN 0018-9480)

(Contents Continued on Back Cover)

(Contents Continued from Front Cover)

Digital Object Identifier 10.1109/TMTT.2008.919703

Application of Millimeter-Wave Radiometry for Remote Chemical Detection

Nachappa Gopalsami, *Senior Member, IEEE*, Sasan Bakhtiari, *Senior Member, IEEE*, Thomas W. Elmer II, *Member, IEEE*, and Apostolos C. Raptis, *Life Member, IEEE*

***Abstract*—Passive millimeter-wave systems have been used in the past to remotely map solid targets and to measure low-pressure spectral lines of stratospheric and interstellar gases; however, its application to pressure-broadened spectral line detection of industrial emissions is new. We developed a radiative transfer model to determine feasibility and system requirements for passive millimeter-wave spectral detection of terrestrial gases. We designed and built a Dicke-switched multispectral radiometer in the 146–154-GHz band to detect nitric oxide (NO), a prototypical gas of nuclear fuel processing operations. We first tested the spectral detection capability of the radiometer in the laboratory using a gas cell and then field tested it at the Nevada test site at a distance of 600 m from a stack that released hot plumes of NO and air. With features such as Dicke-switched integration, frequent online calibration, and spectral baseline subtraction, we demonstrated the feasibility of remote detection of terrestrial gases by a ground-based radiometer.**

***Index Terms*—Chemical detection, millimeter waves, radiometer, remote sensing.**

I. Introduction

WITH RECENT increased concerns about national security has come the realization that acts of nuclear or chemical terrorism could endanger large numbers of people in a short span of time, as could industrial chemical accidents in densely populated areas. In this regard, detection of chemicals in air, especially remotely, is of paramount importance to national security, counterterrorism, leak detection, and environmental protection. It is important also in nuclear counterterrorism efforts since certain chemical effluents from nuclear fuel reprocessing facilities engaged in the production of fuels for nuclear weapons can be the "tell tale" signatures of these operations.

Active and passive spectrometers operating in the optical range have been employed in the past for environmental monitoring and remote sensing applications [1], [2]. Optical systems, which provide superb sensitivity as a consequence of strong molecular absorptions from vibrational transitions, are susceptible to atmospheric effects, and hence, are limited in range of detection. Microwaves and millimeter waves are highly suited for remote sensing applications because of the longer wavelength in relation to cloud and dust particles and less atmospheric attenuation in certain frequency windows.

While active remote sensing techniques based on radar backscattering are routinely used to map out the earth's resources, they are not common for remote chemical detection because of generally weak rotational energy transitions of molecules in the microwave spectrum, but because the rotational absorption increases generally with square of the frequency, active measurement of airborne molecules at millimeter-wave frequencies has been investigated in the past as an extension of laboratory-based spectroscopic techniques [3], [4].

Passive microwave and millimeter-wave techniques have also played an important role in terrestrial remote sensing applications [5]–[7]. Due to the interaction between atoms and molecules, all materials radiate electromagnetic energy. With the radiation spectrum being governed by Planck's radiation law, the sensor output is a linear measure of the temperature of the scene at millimeter wavelengths. A radiometer, which essentially is a highly sensitive receiver, can be used to detect blackbody radiation over a narrow range of the electromagnetic spectrum. Utilizing the excellent contrast of the brightness temperatures of materials, passive millimeter-wave imaging systems, including focal plane imagers, have been developed for detecting objects under optically opaque conditions [8]. In addition, passive millimeter-wave spectroscopy using multispectral radiometers is employed in radioastronomy for detection of interstellar molecules [9]. Radio telescopes are engaged in the detection of narrow molecular emission lines from interstellar molecules against a cold and uniform background, and they generally operate from mountaintop observatories to minimize the atmospheric effects. Also, ground-based radiometers have been used for tropospheric water vapor profiling by measuring the brightness temperatures of the rather strong water vapor line peaks at 22.2 and 183.3 GHz [10], [11].

This paper addresses a ground-based radiometer for passive millimeter-wave detection of chemicals in terrestrial conditions wherein atmospheric attenuation and molecular line broadening effects pose formidable challenges. We will present the design, fabrication, and testing of a passive millimeter-wave spectrometer for remote detection of airborne nitric oxide (NO), which is a prototypical chemical involved in nuclear spent fuel reprocessing. While [12] and [13] have included preliminary results of radiometer modeling, design, fabrication, and proof-of-principle tests in the laboratory, this paper presents comprehensive results of radiometric theory, prototype radiometer design, data acquisition, signal processing, and field test results from the Nevada test site. To the best of our knowledge, this is the first time a ground-based millimeter-wave radiometer has been

Manuscript received August 27, 2007; revised November 8, 2007. This work was supported by the U.S. Air Force.

The authors are with the Nuclear Engineering Division, Argonne National Laboratory, Argonne, IL 60439 USA (e-mail: gopalsami@anl.gov; bakhtiari@anl.gov; elmer@anl.gov; raptis@anl.gov).

Color versions of one or more of the figures in this paper are available online at http://ieeexplore.ieee.org.

Digital Object Identifier 10.1109/TMTT.2008.916985

demonstrated for remote detection of airborne industrial emissions—an important problem to national security and environmental protection.

II. Radiative Transfer Modeling

Based upon the relationship between the brightness and apparent temperatures, the general solution of the radiative transfer equation for a scatter-free atmosphere can be written as [7], [12], [13]

$$T_{DN}(\theta) = T_{BG}e^{-\tau(0,z)\sec(\theta)} + \sec(\theta)\int_0^{\infty} \kappa_a(z')T(z')e^{-\tau(0,z')\sec(\theta)}dz' \quad (1)$$

in which

$$\tau(0,z') = \int_0^{z'} \kappa_a(z)dz. \quad (2)$$

$T_{DN}(\theta)$ is the apparent temperature of the semiinfinite atmosphere observed at a zenith angle θ from a ground-based radiometer, $\kappa_a(z)$ is the absorption coefficient of the atmospheric medium at height z, T_{BG} is the brightness temperature of the background, and $T(z')$ is kinetic temperature of the atmospheric medium at height z'. Under the assumption that each layer is homogeneous, (1) reduces to

$$T_{DN}(\theta;H) = T_{BG}e^{-\tau(0,H)\sec(\theta)} + T_0\left[1 - e^{-\tau(0,H)\sec(\theta)}\right] \quad (3)$$

in which the integration is from $z = 0$ to $z = H$ and the kinetic temperature $T(z) = T_0$. By modeling the atmosphere as a stratified medium made of homogeneous plane layers, (3) can be used to numerically calculate the apparent temperature of the atmosphere. The main millimeter-wave-absorbing molecules in the atmosphere are water vapor and oxygen; in the frequency range of 0–300 GHz, there are water lines at 22.2 and 183.3 GHz and oxygen lines at ~60 GHz (a cluster) and 118.75 GHz. The pressure-broadened absorption coefficients for these lines, for a given water vapor density, were calculated as a function of atmospheric height by using the tabulated values of attenuation parameters in Ulaby *et al.* [5]; oxygen concentration was assumed to be 21% by volume. Fig. 1 depicts the geometry of the detection scenario for an upward-looking radiometer. The target cloud is NO, which emanates from a stack pipe in the form of hot gases. The millimeter-wave absorption coefficient of NO is calculated from the Jet Propulsion Laboratory database [14] and is plotted in Fig. 2 by taking into account pressure broadening. The origin of the lines near 150 and 250 GHz is due to a respective series of $J = 3/2{-}1/2$ and $J = 5/2{-}3/2$ rotational transitions of the $^2\prod$ electronic ground state of NO [15]. The background is assumed to be a mountain with emissivity $\varepsilon < 1$. The atmosphere is divided into three layers with the target plume located in the middle layer. The emission and absorption of each layer are calculated separately and the contribution from all layers is propagated downward to determine the apparent temperature at the radiometer position. Numerical integration is performed for calculating the absorption coefficient in each layer. Using the closed-form solution given in (3), contributions from the upper layer, plume (cloud), and the lower layer, respectively, can be written as

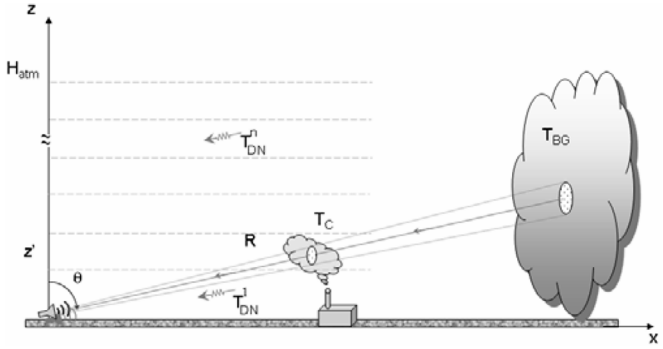

Fig. 1. Geometry of the scene used for the radiative transfer model consisting of gas plume and background within a stratified atmosphere (from [12]).

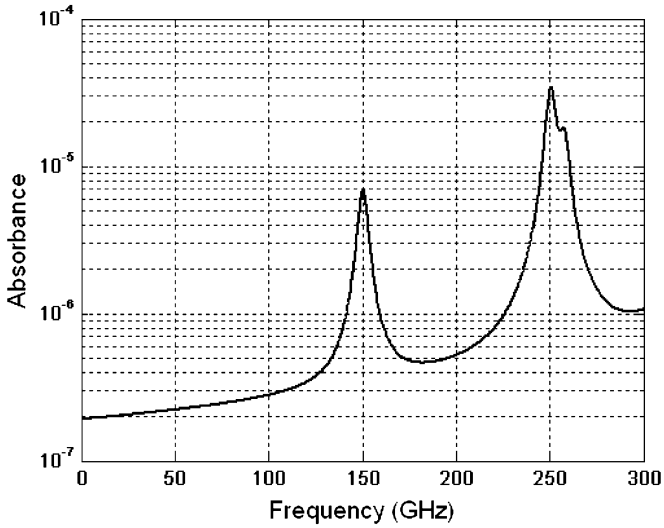

Fig. 2. Pressure-broadened absorption spectra of NO; the results are for 1% by volume of the molecule at 760 torr in 1-cm path length.

$$T_{\rm UL}(\theta) = T_{BG}e^{-\kappa_{\rm UL}z(h+d,H)\sec(\theta)} + T_{\rm atm}\left[1 - e^{-\kappa_{\rm UL}z(h+d,H)\sec(\theta)}\right] \quad (4)$$

$$T_C(\theta) = T_C\left[1 - e^{-\kappa_C z(h,h+d)\sec(\theta)}\right] \quad (5)$$

$$T_{\rm LL}(\theta) = T_{\rm atm}\left[1 - e^{-\kappa_{\rm LL}z(0,h)\sec(\theta)}\right] \quad (6)$$

where h and d are the height and depth of the plume, H is the height of the atmosphere, and $\kappa(\cdot)$ is the absorption coefficient for each layer. The contributions from (4) to (6) may then be combined to determine the apparent temperature at the ground level using

$$T_{DN}(\theta) = T_{\rm LL}(\theta) + \left[T_{\rm UL}(\theta)e^{-\kappa_c z(h,h+d)\sec(\theta)} + T_C(\theta)\right] \times e^{-\kappa_{\rm LL}z(0,h)\sec(\theta)}. \quad (7)$$

Fig. 3 gives the calculated absorption coefficient for standard atmosphere containing oxygen and water-vapor molecules only. To simulate the response of a Dicke-switched radiometer, the

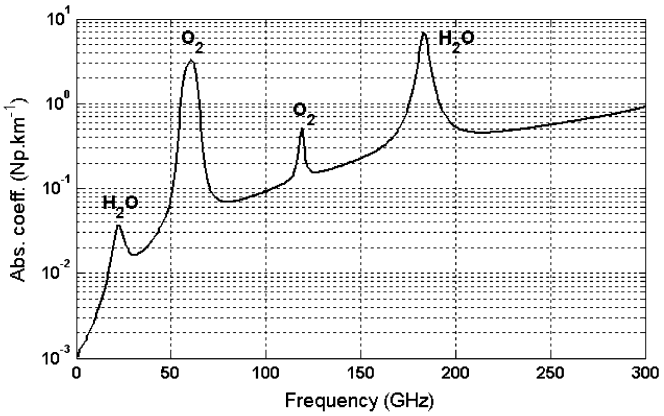

Fig. 3. Absorption coefficient for standard atmosphere containing oxygen and water vapor as a function of frequency. Simulation parameters include $\theta = 0°, H = 2.5$ km, $T_0 = 288.15$ K and $V_{H20} = 7.5$ g $\cdot$ m^{-3} (from [12]).

apparent temperatures in all cases were calculated twice, once without and once with the plume being present. Fig. 4 shows the effect of distance to background on the radiometric temperature at a zenith angle of 84.3°. For the results shown here, the distance to the plume is kept constant, while the distance to the background increases from 5 to 10 km. Although the differential temperature at both peak absorption frequencies declines at larger background distances, the peak at the higher frequency (≈250 GHz) is attenuated by the atmosphere more strongly than the one at lower frequency (≈150 GHz).

As the distance of the ground-based sensor increases from the stack, the viewing angle becomes near horizontal for which the atmosphere would act as a blackbody and ≈≈ the apparent temperature of the sky as a background would be close to the ambient temperature. In this case, if the plume is at ambient temperature $(T_C = T_{BG})$, the difference in temperature with and without the plume against the sky background will be zero. A mountain (with $\varepsilon < 1, T_C < \varepsilon T_{BG}$) behind the plume reduces the path length of the atmosphere and would make a colder background behind the plume.

The modeling results show that: 1) a terrestrial background such as a mountain is almost a necessity for long-range detection of chemical plumes at near ambient temperatures; 2) the expected change in temperature that a radiometer observes from a weakly absorbing plume, such as that of NO, is very small—in the order of tens of millikelvin; and 3) at large standoff distances, the observable signal for NO is stronger for the 150-GHz line than for the 250-GHz line, in spite of the inherently stronger line at the higher frequency.

III. Design and Fabrication of Radiometer

A 16-channel radiometer, covering the frequency range of 146–154 GHz, with 500-MHz bandwidth (BW) per channel, was designed to detect the 150-GHz line of NO. To detect the weak spectral signal of NO, it is necessary to use a Dicke-switching radiometer configuration with long integration times. The minimum detectable temperature of a Dicke-switched radiometer, i.e., ΔT_r, is given by [7]

$$\Delta T_r = \frac{2(T_A + T_R)}{\sqrt{B\iota}} \tag{8}$$

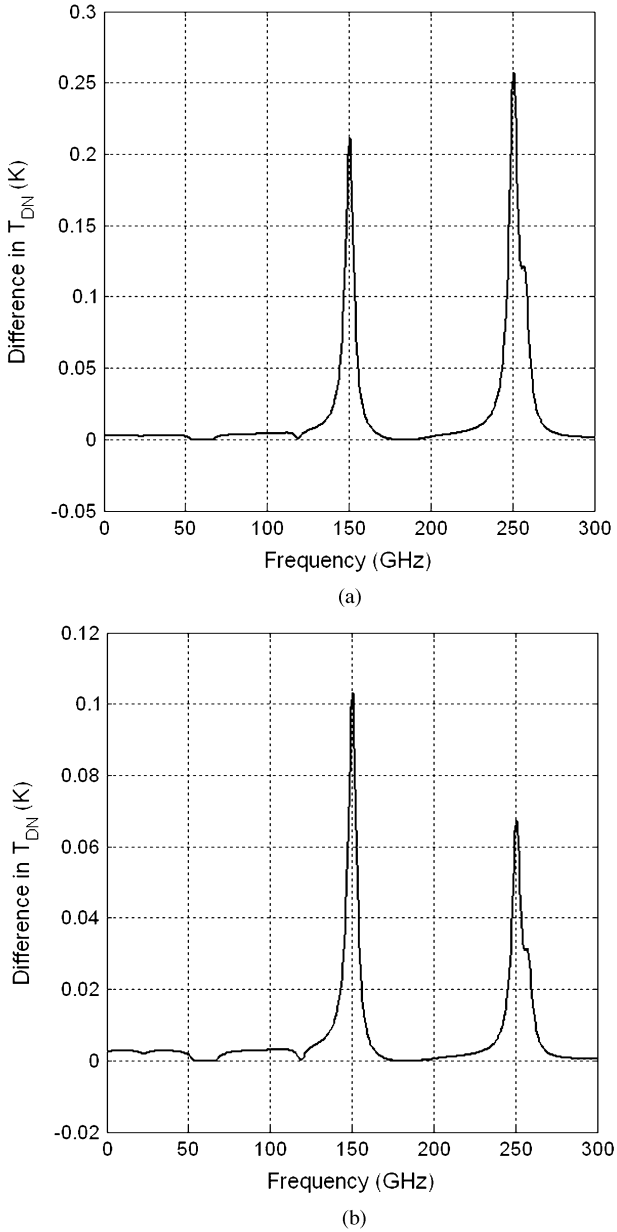

Fig. 4. Difference temperature as a function of frequency for distances to background of: (a) 5 km and (b) 10 km, keeping the target distance constant. For both cases, $h_c = 0.1$ km, $d_c = 0.01$ km, $T_C = 288.15$ K, $\varepsilon = 0.7$, and 1% by volume of NO (from [13]). (a) $\theta = 84.3°, R_C = 1.0$ km, $R_{BG} = 5.0$ km. (b) $\theta = 84.3°, R_C = 1$ km, $R_{BG} = 10$ km.

where T_A is the antenna temperature, T_R is the receiver noise temperature, B is the predetection BW, and ι is the integration time. Using a single-sideband noise figure of 11.9 dB in accordance with vendor quotations for a heterodyne system at 150 GHz, the receiver temperature is $T_R = 4492$ K. With $T_A = 290$ K, $B = 500$ MHz, and $\iota = 600$ s, the minimum detectable temperature from (8) is $\Delta T_r = 16.4$ mK. For this case, the detection sensitivity for NO as derived from Fig. 4(a) is 3.28 parts per thousand. If we use a direct frequency low-noise amplifier (LNA) instead of the heterodyne system, it is possible to obtain an order of magnitude improvement in detection sensitivity. However, an LNA in the 150-GHz range is still not commercially available, but potential exists for it to be built with

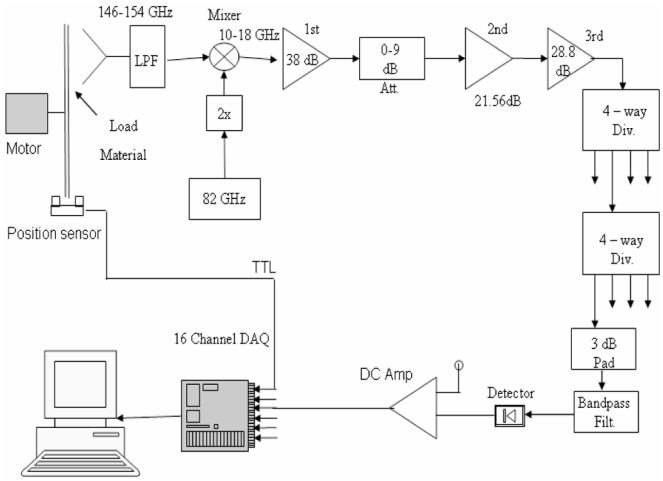

Fig. 5. Schematic diagram of 16-channel passive millimeter-wave spectrometer.

the latest InP-based pseudomorphic high electron mobility transistor technology.

A multispectral radiometer system consisting of millimeter-wave front-end assembly, back-end electronics, and data acquisition hardware and software was assembled as shown in Fig. 5 [12], [13]. A mixer at the front end converts the millimeter-wave frequencies that are centered around a local oscillator frequency of 164 GHz to an IF frequency band of 10–18 GHz; the corresponding RF passband frequencies are 146–154 GHz (lower sideband) and 174–182 GHz (upper sideband). A low-pass filter with a cutoff frequency at ∼160 GHz in front of the mixer passes only the lower sideband signals of interest to the IF band. The IF signal subsequently goes through three stages of amplification. A two-stage four-way power divider splits the signal into 16 channels, each of which goes through a bandpass filter, with the set of filters spanning the 10–18-GHz band with a 500-MHz BW each. The output of each filter is fed to a Schottky barrier diode detector and three stages of video amplifiers to provide video frequency output for the corresponding channel in the form of $S_i = G_i(T_A + T_{Ri})$, where G_i is the gain constant and T_{Ri} is the receiver noise temperature of the ith channel. The video amplifiers contain a precision dc offset correction circuit to nullify the constant value related to $G_i T_{Ri}$ before amplification. The millimeter-wave electronics and the IF filter bank were originally built as a total power radiometer for some other application.

We modified the total power radiometer to operate in a Dicke-switched mode by simply installing an optical chopper in front of the antenna unit and performing the Dicke-switched integration by software. The chopper with its blades coated with an absorber material provides a trigger signal for separating the reference and scene signals. While the conventional Dicke switching is implemented in hardware with a synchronous detection of the reference and scene signals, we have implemented it in software by subtracting and integrating the respective portions of what is effectively two total power radiometer signals for the reference and scene. The two schemes are essentially the same in terms of their signal-to-noise performance, but the latter is prone to thermal drifts of the dc amplifiers.

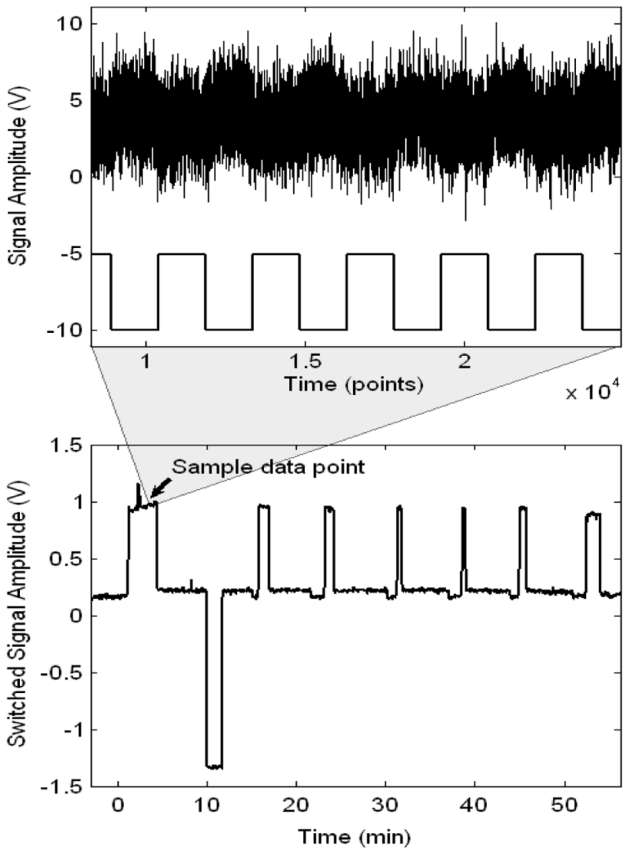

Fig. 6. Single channel output. (*top*) Raw signal of a heat lamp with chopper data. (*bottom*) Dicke-switched integrated signal for a sequence of loads (heat lamp, absorber in liquid nitrogen, and alternating ambient and hot loads).

The video frequency outputs of the radiometer and the synchronization (TTL) signal from the optical chopper are all fed to an 18-bit data acquisition (DAQ) board that is capable of sampling at 500 kS/s. Data collection and Dicke-switched integration of the signals were performed by a LabVIEW program. The data segments were parsed into two parts corresponding to the reference (chopper ON) and scene (chopper OFF) portions, and the two segments were averaged and subtracted from each other to provide a single integrated data point that represents the apparent temperature of the scene. Fig. 6 (*top*), for example, gives a 2-s trace of raw data for one of the channels for a hot load (a ceramic heat lamp at 100 °C) along with the chopper signal. A synchronous integration of the raw signal with the chopper signal over the whole period of 2 s reduces to a single integrated point (∼1 V), as indicated on Fig. 6 (*bottom*), which shows the response of the channel for different loads. Nearly two orders of magnitude improvement in the signal to noise is evident with the 2-s integration. Fig. 6 (*bottom*) gives the response of the channel for various scenes, starting with the ceramic hot load and a cold load (an absorber immersed in liquid nitrogen), followed by alternating scenes of an absorber at ambient temperature and the hot load. The results show the sensitivity and long-term stability of the radiometer to changes in scene temperature.

We next tested the efficacy of long integration times in reducing measurement uncertainty. Fig. 7 gives the measured performance characteristics of individual channels; the rms value of measurement uncertainty is plotted as a function of integration

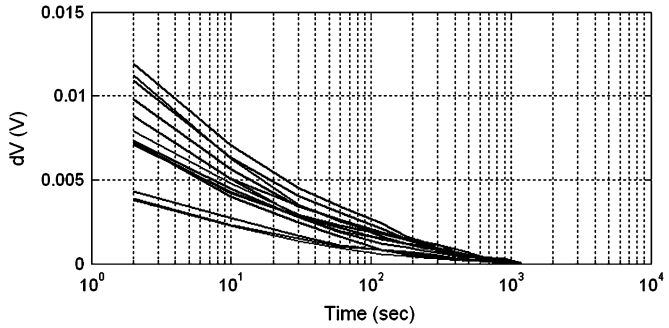

Fig. 7. Root-mean-square deviation of the signal with integration time.

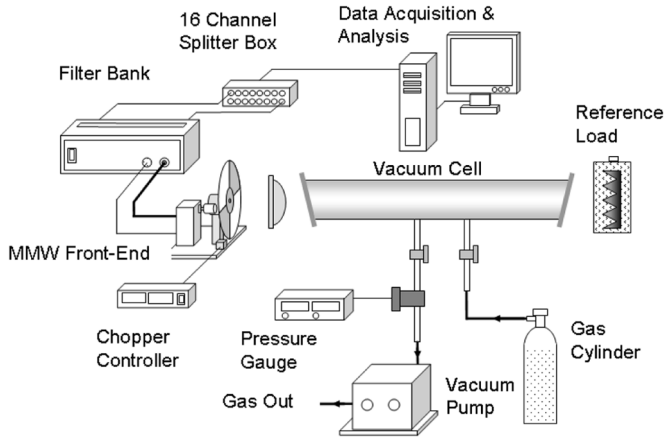

Fig. 8. Laboratory setup for passive measurement of emission spectra of gases at millimeter wavelengths (from [12]).

time in a semilogarithmic scale. As expected, the measurement uncertainty decreases linearly with the square root of integration time for the most part. The slopes of the signals for the various channels vary due to differences in their amplifier gains G_i. Furthermore, the linearity suffers as the integration time becomes large because the dc video amplifiers drift slowly into the nonlinear range, eventually reaching saturation after a few hours.

IV. Proof-of-Principle Testing

To test the proof of principle of passive millimeter-wave spectroscopy, several experiments were conducted by using chemicals with known absorption lines. The laboratory setup for the measurement of emission spectra at millimeter wavelengths is shown in Fig. 8. It mimics the detection scenario in the field, i.e., the radiometer receives the emission signals from a gas in a transparent cell against a thermally contrasting background. Instead of a hot gas against an ambient temperature object in a field scenario, here we use an ambient temperature gas against a cold background. Measurement was made with a 30-s integration time and over a ∼30-min time span. The normalized radiometer response for a hot load (time interval from 0 to ∼5 min), human hand (time intervals centered at ∼7 and ∼15 min), and CH_3CN vapor (centered at ∼10 and ∼20 min) is given in Fig. 9(a) and the corresponding spectral image in Fig. 9(b). While all channels show the same normalized response for uniform loads such as the hot load and hand, the response pattern changes when CH_3CN is introduced into

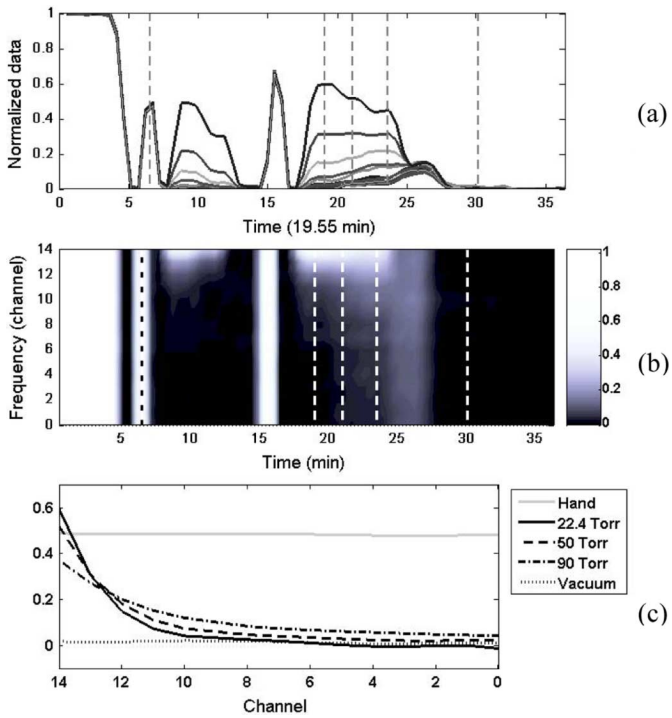

Fig. 9. Display of laboratory measurement results for hot load, hand, and CH_3CN gas at various pressures. (a) Normalized data for all channels. (b) Spectral image of the various scenes. (c) Spectra at marked time instances.

the cell due to its emission spectra. Typical frequency responses of the channels for hand and CH_3CN at various pressures are shown in Fig. 9(c); the channel numbers 15-0 correspond to the frequency range of 146.25–153.75 GHz in 0.5-GHz intervals. To test the pressure broadening effect, we mixed nitrogen to CH_3CN at 22.4 torr; the line broadening and dilution effects are clearly seen in the spectral responses for CH_3CN–nitrogen mixtures at 60 and 90 torr.

Since the rotational spectra of CH_3CN are known and can be obtained from molecular spectral databases such as that of the Jet Propulsion Laboratory [14], we can calculate its emission spectra for a temperature difference of 223 K and compare it with the measured spectrum. CH_3CN is a symmetric top and there are several strong K-type $J = 8_K - 7_K$ transitions at 147 GHz, which will broaden with pressure and occupy the lower end channels near 146 GHz. Fig. 10 gives the calculated and measured emission spectra for 5% CH_3CN at 1 torr. While the agreement is fairly good at high signal (emission) levels, the channel fluctuations become obvious at low-signal levels. This finding shows that extreme care must be taken to bring down these uncertainties by frequent calibration, channel normalization, signal integration, and baseline subtraction.

V. Field Testing

Fig. 11 sows the test scenario at the Nevada test site in which a hot plume of air or NO at 140 °C was released from a 21.95-m-high stack of internal diameter 0.5 m. The spectrometer was situated in a trailer 600 m away from the stack in the crosswind direction, and it was pointed through a transparent window to the plume near the top of the stack against the background of a mountain approximately 8 km behind the stack. The outside temperature, during tests, was from 43 °C to 46 °C; the wind

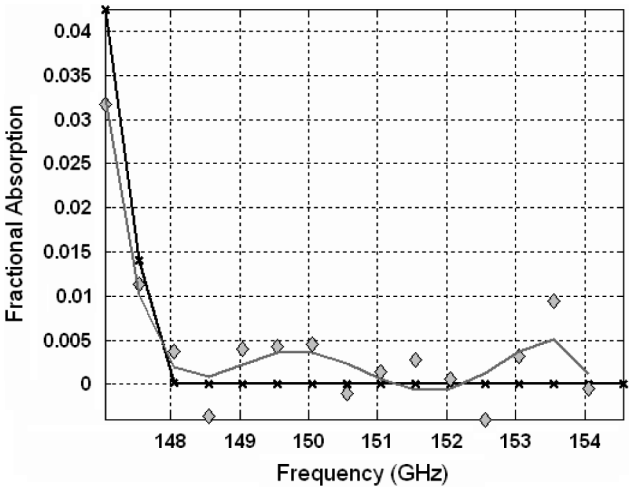

Fig. 10. Comparison of measured (◇) and simulated (*) spectra for 5% CH_3CN at 1 torr (from [13]).

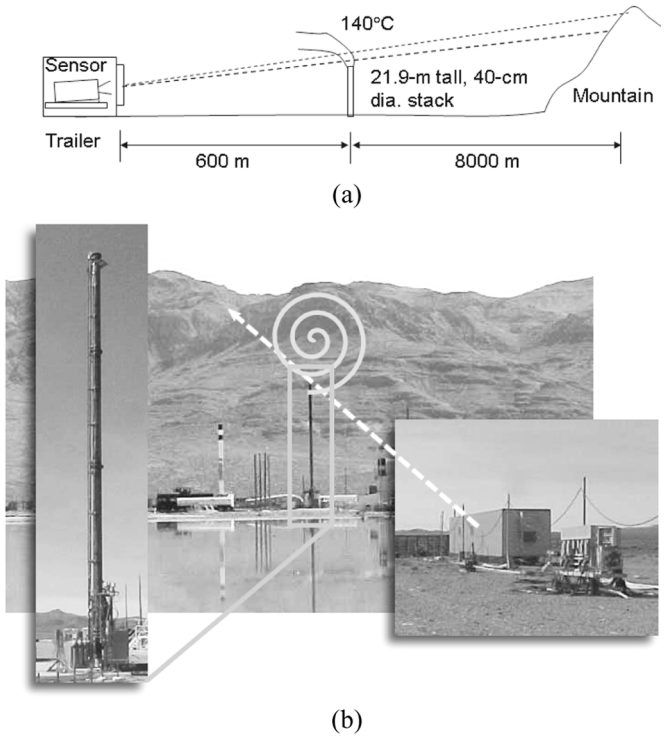

Fig. 11. Field test scenario at the Nevada test site. (a) Schematic diagram. (b) Photograph of the scene.

was blowing hard at times and the relative humidity was higher than normal, ∼40% because of the prevailing monsoon season. A Fourier transform infrared (FTIR) instrument was mounted at the top of the stack to provide an *in-situ* quantitative measurement of the released NO levels.

The laboratory unit was modified for the field tests as follows. To improve the fill factor of the antenna footprint on the plume, a 0.3-m lens antenna was installed and matched to the scalar horn of the radiometer (see Fig. 12). The (3 dB) beamwidth of the lens was 0.47°, which provides a footprint of 4.9 m at a distance of 600 m. The entire radiometer assembly was mounted on rotational and tilting platforms to align along azimuth and elevation. A pointing telescope was also mounted on top of the receiver in parallel with the lens axis for visually aligning the

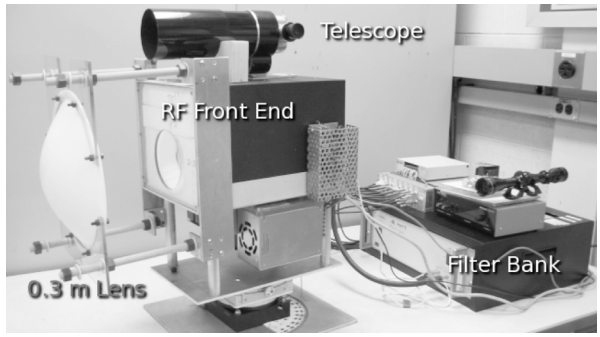

Fig. 12. Field setup of passive millimeter-wave spectrometer system.

lens antenna on the target. The whole RF front-end assembly was thermally isolated and cooled by a thermoelectric cooler to maintain the radiometer front end at a constant temperature (12 °C), which would help minimize the drift of the channel gains.

A radio beacon at 150 GHz (frequency multiplied IMPATT source with a horn antenna) was used at the foot of the stack to further refine the alignment of the lens antenna on the target. With the radio beacon at the foot of the stack and aimed toward the receiver (with a strong attenuator in the front of the horn to avoid saturating the receiver), we aligned the receiver antenna for maximum signal while the telescope was adjusted to point at the antenna horn of the beacon. This alignment should hold good for that fixed radius; hence, the telescope view can be used for aiming the receiver to the top of the stack. We next tested the radiometer readouts of the scenes around the stack. Fig. 13 shows the apparent temperatures of a sequence of scenes: an absorber in front of the antenna, the ground, middle, and top parts of the stack, and the sky at the viewing angle (near horizon) of the top of the stack; they were calculated on the basis of the hot and cold load temperatures. The mountain appears colder than the ground; the sky appears colder than the mountain for the short (600 m) range, but the sky temperature will increase as the range and the zenith angle increases. Note that the horizontal lines between the object signals represent breaks in the data collection. The channel gains drift increasingly as a function of time, thus necessitating frequent calibration and gain normalization. For this, we devised two constant temperature loads: a blackbody absorber (honeycomb) at ambient temperature and a ceramic heat lamp with a constant temperature of 100 °C. These loads would be precisely positioned in front of the lens every 5 min for calibration.

The acquisition and real-time analysis of the radiometric data were performed under the LabVIEW environment. The virtual instrument interface of the acquisition software was developed to simultaneously collect data from all 16 channels of the radiometer. The primary functions of the software include simultaneous acquisition and recording of raw data, real-time reference subtraction, instantaneous display of spectral lines across frequency channels, options to save the original and differential traces, dynamic calibration, creating event markers for post-test analysis, and monitoring and saving temperature data from the cooling system. The LabVIEW interface was optimized to provide real-time processing and display of the spectral data; even

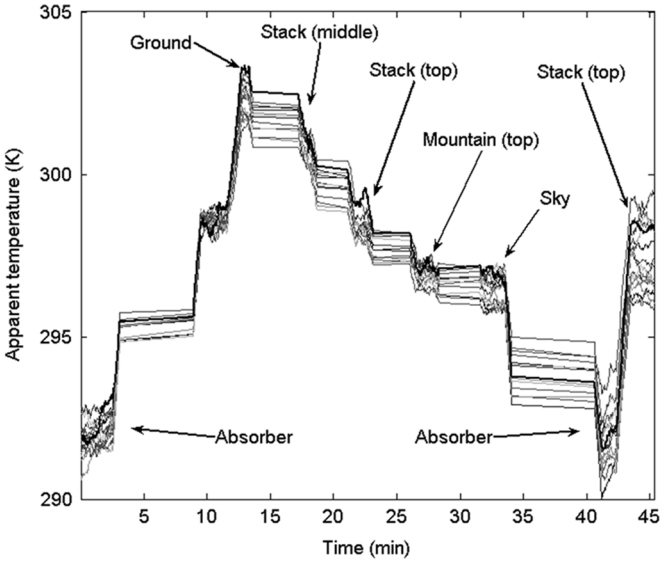

Fig. 13. Thermal signatures of objects around the measurement stack.

so, it was not fast enough, without losing any data record from the DAQ board, to detect radiometric temperature variations for weakly emitting/absorbing molecules in real time. Therefore, additional postprocessing of data was devised to achieve the necessary level of sensitivity.

A series of algorithms were implemented in MATLAB programming language for post processing of the radiometric data. To simplify the operations, the scripts were later integrated into a graphical user interface (GUI). Radiometric data may be processed and displayed by the GUI in various formats including time trace, spectrograph, and frequency cross-section profile, as shown in Fig. 9. Main postprocessing steps of the data, which are aimed at detecting the spectral line of a target chemical in the plume, are listed as follows:

1) gain normalization;
2) spectral baseline subtraction;
3) integration in time;
4) temporal baseline subtraction;
5) aggregation of channels for signal enhancement.

The multichannel radiometer output of the scene, given by (7), is a function of time t and spectral line frequency f, and it may be simplified by neglecting atmospheric attenuation as

$$T_{DN}(t,f) = [T_{BG}(t) - T_C(t)] \exp[-\alpha(f)Cd] + T_C(t) \quad (9)$$

where C is the concentration of the target chemical and $\alpha(f)$ is the Lorentzian line shape function of the spectral line [3]

$$\alpha(f) = \frac{A\delta f}{(f-f_0)^2 + (\delta f)^2} \quad (10)$$

in which A is the integrated line peak and δf is the linewidth (see Fig. 2). The discrete time output for a 15-channel (the 16th channel is used for trigger data from the chopper) radiometer is given by

$$S(i,j) = [T_{BG}(i) - T_C(i)] \exp[-\alpha(j)Cd] + T_C(i), \quad i = 1,2,\ldots,N; \quad j = 1,2,\ldots,15. \quad (11)$$

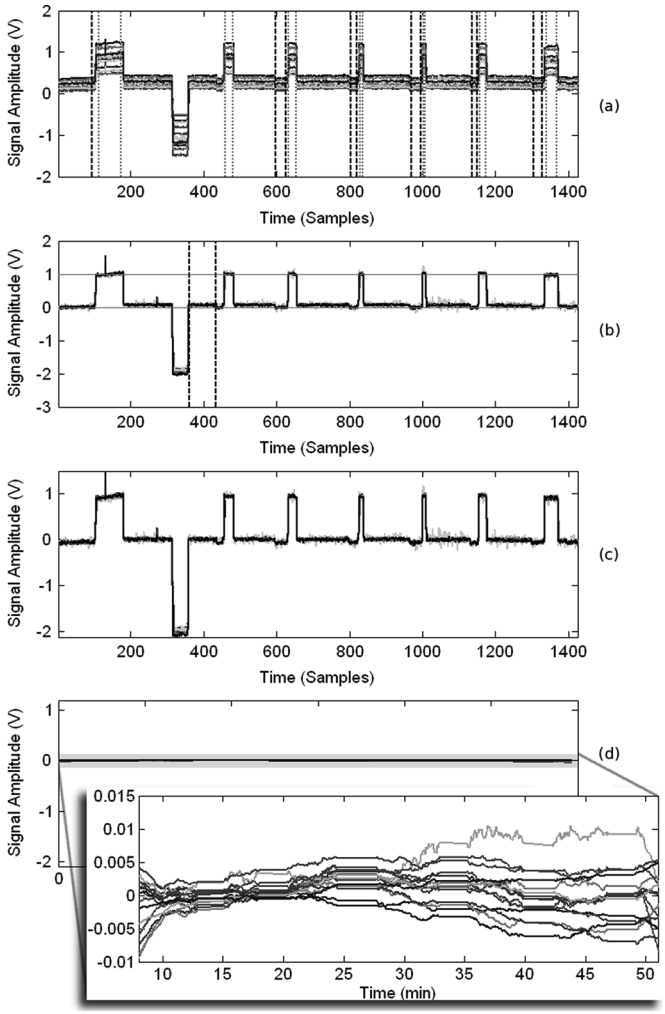

Fig. 14. Signal processing steps illustrated with multichannel output for a plume release with periodic calibration using hot and cold loads. (a) Dicke-switched raw data of all channels with different gains. (b) Gains normalized with hot and clod load responses. (c) Spectral baseline subtracted before the release of the plume. (d) Temporal baseline subtracted to mitigate atmospheric fluctuation.

Fig. 14(a) shows a time trace (amplitude versus data bin) over a 60-min time period of all 15 frequency channels for a reference scene above the stack; the step changes indicate hot and ambient temperature loads used for calibration. First, the amplitudes of all channels are independently normalized to adjust for gain variations among the channels [see Fig. 14(b)]. The scaling factors are calculated based on the hot and cold loads used in calibration.

The second step is spectral baseline subtraction, which consists of subtracting the plume spectra from the reference spectra at time $i = i_1$ before the start of the target gas

$$S_{\rm sb}(i,j) = S(i,j) - S(i_1,j). \quad (12)$$

For time $i > i_1$ and C small, (12) becomes

$$S_{\rm sb}(i,j) \approx [T_C(i) - T_{BG}(i)]\alpha(j)Cd, \qquad \text{for } i > i_1. \quad (13)$$

Fig. 14(c) gives the spectral baseline subtracted data. Ideally the radiometer data (in between calibration points) should display

only the spectral data, proportional to the line strength and the difference temperature between the plume and background.

In the third step, all the data traces are integrated by using a moving average filter (integration step); the filter parameters are selected based on the integration time needed. This step averages out the temporal fluctuation and reduces noise.

The fourth step is temporal baseline subtraction in which the time trace of the beginning frequency channel is subtracted from the remainder of the frequency channels

$$S_{\rm tb}(i,j) = S_{\rm sb}(i,j) - S_{\rm sb}(i,1) \approx \Delta T \alpha(j) CD \quad (14)$$

where $\Delta T = T_C(i) - T_{BG}(i)$.

Since atmospheric fluctuation affects all channels equally within the BW, this step of subtracting the beginning channel data from the remainder of the channels compensates for atmospheric fluctuation. Fig. 14(d) gives the temporal baseline corrected data. From (14), the processed data should show zero values for all channels before the NO release (during the reference scene) because α is zero during the reference scene and should show the NO spectral spread during the NO release. A comparison of spectral data at times of hot air and NO releases show a closely spaced spectral data for hot air (middle portion) and spread out spectral data during the NO release (end portion). Note that the calibration scene is also subtracted out in this step. Some of the channel spread in the beginning and end portions is due to a lack of data points in an n-point moving average.

To enhance detection potential for a chemical with known spectral line shape, we implemented a postprocessing routine into the MATLAB GUI to arbitrarily aggregate frequency channels. This routine may be used, for instance, to aggregate the frequency channels around a spectral peak and those around its tails and subtract the two to bring out the maximum difference. This two-point difference detection scheme increases the detection potential for weak spectral signals.

Figs. 15 and 16 present the detection results for an NO release mixed in air at a temperature of 140 °C at 4620 ppm, and Fig. 17 that at 2852 ppm. The release sequence in the first release consisted of hot air release for 20 min, followed by four releases of NO mixed with air in 5-min stretches with a 2-min break in between the releases for calibration. Since the NO line peaks in the middle of the BW and flattens to zero at the ends (Fig. 2), the probability of detection may be improved by the two-point difference detection scheme of summing the five central channels and subtracting the sum of ten outer channels. Fig. 16 shows the result of this two-point difference detection for a 15-min integration; the inset (arbitrarily scaled) provides the FTIR data from the stack-mounted system, showing the time sequence of the NO release and its concentration. The two-point data clearly indicates the difference in signal for NO and air. The NO signal appears extended on both sides of the start and stop of the release because of the 15-min moving average filter.

Fig. 16 depicts the results of model-fitted data of the first release (corresponding to 4620 ppm) using all channels, based on a least squares fit of the NO line shape with the frequency profile data. Fig. 16(a) gives the best fitted line peak for air and NO data as a function of time, Fig. 16(b) is the frequency image

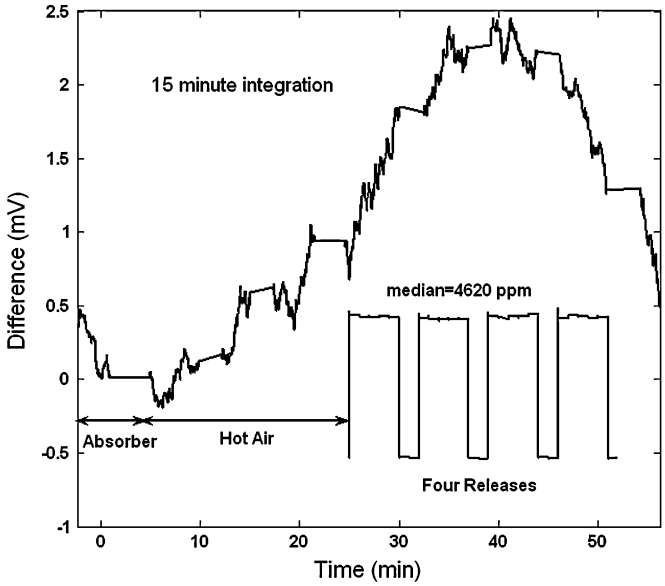

Fig. 15. Detection of NO at 4620 ppm: difference between the central and outer channels.

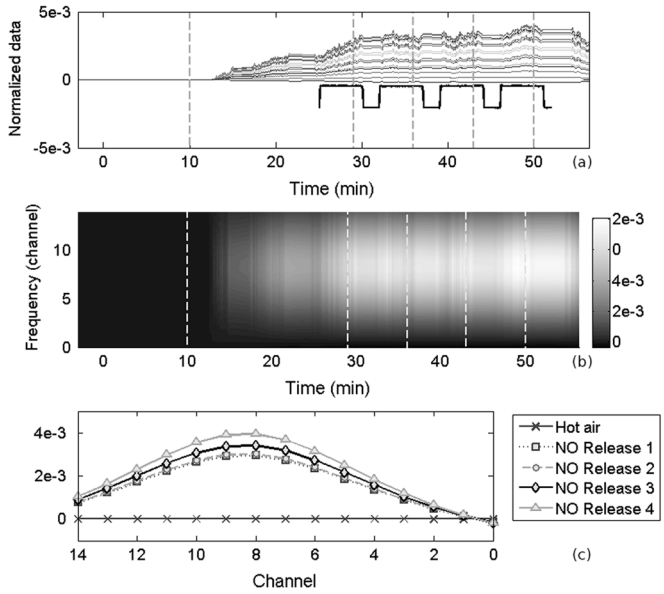

Fig. 16. Model-fitted data of NO release at 4620 ppm. (a) Normalized data. (b) Spectral image. (c) Frequency profiles at various time instances.

of the data in Fig. 16(a), and Fig. 16(c) gives typical responses of model-fitted spectral lines of NO at various time instances. The model-fitted data analysis indicates better detection potential for the case of detecting the presence of a known chemical in a plume.

With the two-point difference detection analyses used in Fig. 15, but with a 5-min integration time, the detected trace for second release at 2852 ppm of NO in air is given Fig. 17. The release sequence consisted of 18 min of hot air, 9 min of intermittent puffs of NO, and 10 min of NO at 2852 ppm. Once again, the two-point difference plot shows the times of NO release clearly, although with a lower signal-to-noise ratio than of Fig. 15, which had a higher release concentration.

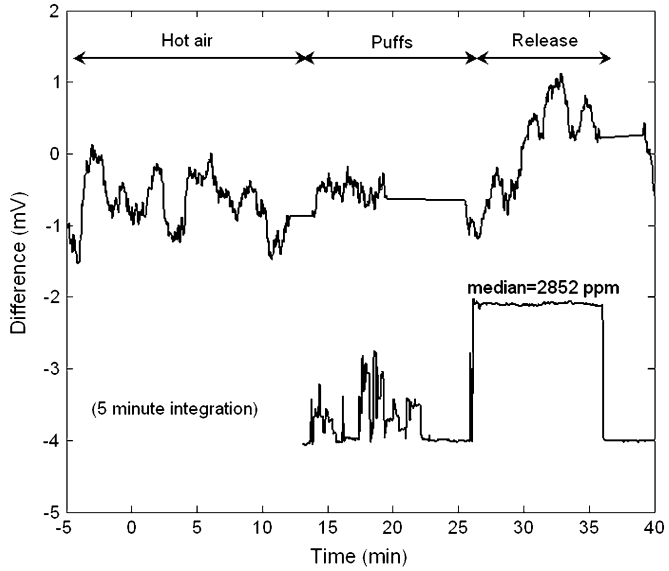

Fig. 17. Detection of NO at 2852 ppm: difference between the central and outer channels.

The detection sensitivity of the system can be improved many fold by minimizing the drift in the video amplifier part of the receiver. We have implemented 16 IF channels by power splitters and filters, each channel having its own diode detector and dc amplifier chain. The main uncertainty in the spectral data has been the drift of these individual channels having different diode responses and video amplifier gains and offsets. The dc amplifiers drifts may be frequently zeroed out manually and calibrated often, or the filter bank may be kept in a thermally controlled environment to minimize the amplifier drifts, which are mostly thermal in nature. It is also possible to calibrate out these uncertainties along with any nonlinearities by using precision noise injection in the RF stage [10]. Another option is to implement the synchronous detection between the reference and scene signals in hardware and using ac-coupled amplifiers, as is done in the conventional Dicke switching. With such improvement and frequent calibration, we believe the system can detect NO, which is inherently a weak absorber (10^{-4} cm^{-1}) to a 100-ppm sensitivity level. Note for molecules with stronger dipole moments such as hydrogen sulfide (10^{-2} cm^{-1}) and hydrogen cyanide (10^{-1} cm^{-1}), the current system as such is capable of detecting 1–10 ppm.

VI. Conclusion

We have designed and developed a remote sensing radiometer for spectroscopic detection of airborne chemicals from a facility's stack. A radiative transfer model was developed to simulate the expected radiometric signals for typical terrestrial remote sensing scenarios. The simulation results showed the feasibility of detecting polar gases such as NO from a few kilometers using a state-of-the-art radiometer with a long integration time (up to 10 min). A Dicke-switched radiometer was built to measure the 150-GHz spectral line of NO between 146–154 GHz with 16 channels having 500-MHz BW per channel. The proof of principle was tested in the laboratory by passively measuring a spectral line of CH_3CN vapor in a gas cell against the background of a liquid-nitrogen load. The measured spectra agreed well with the calculated spectra of CH_3CN.

The spectrometer front end was fitted with a lens antenna and mounted on a tilting and swivel platform for field tests. A LabVIEW-based data acquisition and signal processing software was developed to allow gain normalization, dynamic calibration, baseline subtraction, signal integration, and spectral data display. MATLAB-based postprocessing software was also developed to allow temporal and spectral baseline subtraction, channel aggregation, and model-fitted spectral data processing. The radiometer, located in a trailer, 600 m away from a release stack at the Nevada test site detected NO releases of a few parts per thousand in air. The main uncertainty in the spectral data has been the drift of the individual IF channels having different diode responses and video amplifier gains and offsets. This uncertainty may be reduced in the future design by implementing either the noise injection scheme to calibrate out the uncertainties or the synchronous detection part of the Dicke-switching in hardware, which allows the use of ac-coupled amplifiers. With such improvement and frequent calibration, we believe the system can detect NO, which is inherently a weak absorber (10^{-4} cm^{-1}) to a 100-ppm sensitivity level. Application of spectroscopic techniques for passive detection of terrestrial gases at millimeter-wave frequencies is a new frontier in science and the offshoots of this technology are expected in the future to have industrial, scientific, and medical applications.

Acknowledgment

The authors wish to thank H. Murakami, University of California at Berkeley, and R. Lanham, Argonne National Laboratory, Argonne, IL, for their technical assistance.

References

[1] R. Wainner, M. Frish, and M. Allen, "Hydrocarbon gas sensing using 3.5 micron type II interband cascade lasers," *Lasers Electro-Opt.*, vol. 1, pp. 1–2, 2004.

[2] T. Tarumi, G. W. Small, R. J. Combs, and R. T. Kroutil, "High-pass filters for spectral background suppression in airborne passive Fourier transform infrared spectrometry," *Anal. Chem. Acta*, vol. 501, pp. 235–247, 2004.

[3] N. Gopalsami and A. C. Raptis, "Millimeter-wave radar sensing of airborne chemicals," *IEEE Trans. Microw. Theory Tech.*, vol. 49, no. 4, pp. 646–653, Apr. 2001.

[4] N. Gopalsami, A. C. Raptis, and J. Meier, "Millimeter-wave cavity ringdown spectroscopy," *Rev. Sci. Instrum.*, vol. 73, pp. 259–262, 2002.

[5] F. T. Ulaby, R. K. Moore, and A. K. Fung, *Microwave Remote Sensing: Active and Passive, Vol. I—Microwave Remote Sensing Fundamentals and Radiometry*. Reading, MA: Addison-Wesley, 1981.

[6] L. Yujiri, M. Shouri, and P. Moffa, "Passive millimeter-wave imaging," *IEEE Micro.*, vol. 4, no. 3, pp. 39–50, Sep. 2003.

[7] M. A. Janssen, Ed., *Atmospheric Remote Sensing by Microwave Radiometry*. New York: Wiley, 1993.

[8] N. Gopalsami and A. C. Raptis, R. M. Smith, Ed., "Millimeter-wave imaging of thermal and chemical signatures," in *Proc. SPIE Passive Millimeter-Wave Imag. Technol. III Conf.*, 1999, vol. 3703, pp. 130–138.

[9] J. M. Payne, "Millimeter and submillimeter wavelength radioastronomy," *Proc. IEEE*, vol. 77, no. 7, pp. 999–1017, Jul. 1989.

[10] J. B. Snyder, , D. Solimini, Ed., "Observed and theoretical atmospheric emission at 20, 30, and 90 GHz: Recent results from land- and ocean-based locations," in *Microwave Radiometry and Remote Sensing of the Environment*. Zeist, The Netherlands: VSP, 1995.

[11] Y. Han and E. Westwater, "Remote sensing of tropospheric water vapor and cloud liquid water by integrated ground based sensors," *J. Atmos. Ocean. Technol.*, vol. 12, pp. 1050–1059, 1995.

[12] N. Gopalsami, S. Bakhtiari, T. W. Elmer, and A. C. Raptis, "Remote detection of chemical plumes with passive millimeter waves," *Proc. SPIE*, vol. 6378, pp. A1–A12, 2006.
[13] S. Bakhtiari, N. Gopalsami, T. W. Elmer, and A. C. Raptis, "A millimeter wave radiometer for terrestrial remote sensing of chemical plumes," in *Proc. 3rd Int. Electromagn. Near-Field Imag. Characterization Conf.*, St. Louis, MO, Jun. 27–29, 2007, pp. 141–146.
[14] R. L. Poynter and H. M. Pickett, *Spectral Line Catalog*. Pasadena, CA: Jet Propulsion Lab., 1983, vol. 80–23.
[15] C. H. Townes and A. L. Schawlow, *Microwave Spectroscopy*. New York: Dover, 1975.

Nachappa (Sami) Gopalsami (S'80–M'80–SM'95) received the B.E. and M.S. degrees in electrical engineering from the University of Madras, Madras, India, and Ph.D. degree in electrical engineering and computer science from the University of Illinois at Chicago.

In 1980, he joined Argonne National Laboratory, Argonne, IL, where he is currently a Senior Electrical Engineer with the Sensors and Instrumentation Section, Nuclear Engineering Division. He has authored or coauthored over 150 technical papers in the area of sensors and nondestructive evaluation (NDE). He holds five U.S. patents. His current research interests include development of RF, microwave, millimeter-wave, and terahertz sensors and imaging systems for national security, biosensing, environmental monitoring, and materials applications.

Dr. Gopalsami is a member of Sigma Xi and SPIE. He was the recipient of two Research and Development (R&D) 100 Awards presented by *R&D Magazine* (both on millimeter-wave sensors, 1986 and 2007), an Outstanding Paper Award presented by the American Society of Nondestructive Testing, and an Outstanding Mentor Award presented by the Office of Science Undergraduate Research Programs.

Sasan Bakhtiari (S'92–M'91–SM'94) received the B.S.E.E. degree from the Illinois Institute of Technology, Chicago, in 1983, the M.S.E.E. from the University of Kansas, Lawrence, in 1987, and the Ph.D. degree in electrical engineering from Colorado State University, Fort Collins, in 1992.

From 1984 to 1987, he was with the Radar Systems and Remote Sensing Laboratory, University of Kansas. From 1998 to 1992, he was with the Microwave Nondestructive Testing Laboratory, Colorado State University. In 1993, he joined Argonne National Laboratory, Argonne, IL, where he is currently an Electrical Engineer with the System Technologies and Diagnostics Department, Nuclear Engineering Division. He is also the Section Manager for the Nondestructive Evaluation (NDE) Section. He has authored or coauthored numerous technical publications in the areas of sensors and NDE. He holds four U.S. patents. His current research interests include active and passive microwave, RF, and induction sensing technologies for scientific and industrial applications.

Dr. Bakhtiari was the recipient of two Research and Development (R&D) 100 Awards presented by *R&D Magazine* and an Outstanding Paper Award presented by the American Society for Nondestructive Testing.

Thomas W. Elmer II (M'07) received the B.S. degree in physics (with minors in math and computer science) from La Sierra University, Riverside, CA, in 1998, and the M.S. degree from the University of Illinois at Chicago, in 2004.

While with La Sierra University, he was with the Physics Department, where he was involved with writing and maintaining programs to run laboratory experiments. He has also lectured on astronomy and gravitational physics for the Physics Department. His senior research project was with the Health Physics Department, Loma Linda University Medical Center, for which he analyzedthe activation of Cerrobend(R) metal by 250-MeV protons at the hospital's Proton Facility. In 1999, he joined Argonne National Laboratory, Argonne, IL, as a Student Intern, eventually remaining as a Special Term Appointee for the System Technologies and Diagnostics Department, Nuclear Engineering Division. He writes programming for modeling, motion control, data acquisition, and data analysis in the microwave, millimeter-wave, and terahertz sensors laboratories.

Mr. Elmer was the recipient of the 2007 Research and Development (R&D) 100 Award presented by *R&D Magazine*.

Apostolos C. Raptis (S66–M'67–LM'06) received the Ph.D. degree in electrical engineering from the University of Akron, Akron, OH, in 1973.

He was initially a Research Engineer for the Gulf Research and Development Company. In 1974, he joined Argonne National Laboratory, Argonne, IL, where he is currently a Senior Electrical Engineer and the Department Manager for Systems Technologies and Diagnostics with the Nuclear Engineering Division. His areas of expertise include sensors, instrumentation and controls, nondestructive evaluation, data processing, electromagnetics, plasmas, optics, acoustics, and geophysical exploration. During his tenure with Argonne National Laboratory, he has also been an Adjunct Professor with the Electrical Engineering Department, University of Illinois at Chicago. He is currently on the Advisory Board for the Electrical Engineering Department of the University of Akron and University Miami of Ohio. He has authored over 250 publications. He holds 17 U.S. patents.

Dr. Raptis was the recipient of the 1994, 1996, and 2007 Research and Development (R&D) Award and a 1994 American Society for Nondestructive Testing (ASNT) Best Paper Award.